Prospective dark matter annihilation signals from the Sagittarius Dwarf Spheroidal

Venville, T.A.A.; Duffy, A.R.; Crocker, R.M.; Macias, O.; Tepper-Garcia, T.

Prospective dark matter annihilation signals from the Sagittarius Dwarf Spheroidal

Thomas A. A. Venville [1,2]★ Alan R. Duffy [1,2] Roland M. Crocker [3] Oscar Macias [4,5] and
Thor Tepper-García [6,7]

[1]*Centre for Astrophysics and Supercomputing, Swinburne University of Technology, PO Box 218, Hawthorn, Victoria 3122, Australia*
[2]*ARC Centre of Excellence for Dark Matter Particle Physics, Australia*
[3]*Research School of Astronomy and Astrophysics, Australian National University, Canberra 2611, A.C.T., Australia*
[4]*Department of Physics and Astronomy, San Francisco State University, San Francisco, CA 94132, USA*
[5]*GRAPPA – Gravitational and Astroparticle Physics Amsterdam, University of Amsterdam, Science Park 904, NL-1098 XH Amsterdam, the Netherlands*
[6]*School of Physics, Sydney Institute for Astronomy, The University of Sydney, NSW 2006, Australia*
[7]*Centre of Excellence for All Sky Astrophysics in Three Dimensions (ASTRO-3D), Australia*

ABSTRACT
The Sagittarius Dwarf Spheroidal galaxy (Sgr) is investigated as a target for dark matter (DM) annihilation searches utilizing J-factor distributions calculated directly from a high-resolution hydrodynamic simulation of the infall and tidal disruption of Sgr around the Milky Way. In contrast to past studies, the simulation incorporates DM, stellar and gaseous components for both the Milky Way and the Sgr progenitor galaxy. The simulated distributions account for significant tidal disruption affecting the DM density profile. Our estimate of the J-factor value for Sgr, $J_{\rm Sgr} = 1.48 \times 10^{10}$ M$_\odot^2$ kpc^{-5} (6.46×10^{16} GeV cm^{-5}), is significantly lower than found in prior studies. This value, while formally a lower limit, is likely close to the true J-factor value for Sgr. It implies a DM cross-section incompatibly large in comparison with existing constraints would be required to attribute recently observed gamma-ray emission from Sgr to DM annihilation. We also calculate a J-factor value using a NFW profile fitted to the simulated DM density distribution to facilitate comparison with past studies. This NFW J-factor value supports the conclusion that most past studies have overestimated the dark matter density of Sgr on small scales. This, together with the fact that the Sgr has recently been shown to emit gamma-rays of astrophysical origin, complicate the use of Sgr in indirect DM detection searches.

Key words: astroparticle physics – galaxies: individual: Sagittarius Dwarf – dark matter – gamma-rays: galaxies.

1 INTRODUCTION: DARK MATTER ANNIHILATION SIGNALS FROM DWARF SPHEROIDAL GALAXIES

In the Λ cold dark matter cosmological model of our Universe, approximately 83 per cent of the total mass density of the Universe consists of dark matter (DM), a massive particle species that primarily interacts with baryonic matter through gravitational interactions (Garrett & Dūda 2011). The hierarchical gravitational formation of structure in this cosmological model results in galaxies contained in more massive DM haloes. These DM haloes are thus often traced by stellar populations. Diverse experiments have attempted to detect particle DM candidates, targeting a wide range of DM masses and velocity averaged annihilation cross-sections (e.g. Bertone, Hooper & Silk 2005). These experimental searches include monitoring for direct detection of DM interaction with target materials and 'indirect' searches for Standard Model products of DM self-annihilation and decay, for example gamma-rays, neutrinos, and charged cosmic rays.

These experiments have, thus far, not (definitively) detected DM particle candidates.

Dwarf spheroidal galaxies are promising targets for DM searches due to their high mass to light ratios (indicating an abundance of dark matter). Indirect dark matter searches for products of dark matter annihilation in dwarf spheroidal galaxies and the Galactic Centre have been conducted with a variety of observational facilities targeting different areas of particle parameter space. Claims of detection of a gamma-ray spectral line signature (Bringmann & Weniger 2012) and potential continuum emission (Goodenough & Hooper 2009; Gordon & Macías 2013; Abramowski et al. 2014) due to Weakly Interacting Massive Particles (WIMP) dark matter annihilation from dwarf spheroidal galaxies have been made. However, the fact that such claimed gamma-ray signatures have been, at best, similar in magnitude to astrophysical gamma-ray backgrounds – which are themselves somewhat uncertain – has so far precluded conclusive identification of observed gamma-ray fluxes as products of dark matter annihilation (Abramowski et al. 2014; Calore et al. 2015; Geringer-Sameth, Koushiappas & Walker 2015; Macias et al. 2018, 2019; Abazajian et al. 2020; Pohl et al. 2022).

★ E-mail: 101615311@student.swin.edu.au

Compared to the Galactic Centre region and 'classical' dwarf spheroidal (dSph) galaxies, which have been investigated extensively for indirect signatures of dark matter annihilation, few prior studies have previously investigated the Sagittarius Dwarf Spheroidal Galaxy (Ibata et al. 1997; Aharonian et al. 2008; hereafter Sgr) as a target for dark matter annihilation searches. This is due to the location of Sgr near the Galactic plane and Galactic Centre region,[1] uncertain astrophysical background sources (Viana et al. 2012; Crocker et al. 2022), and large systematic uncertainties in the dark matter distribution (and thus the spatial morphology of any dark matter annihilation signature) of Sgr due to ongoing tidal disruption (Rico 2020). The most significant continuum detection of gamma-ray emission from Sgr was made by Crocker et al. (2022), who detect Sgr with an $8.1\,\sigma$ significance in Fermi Large Area Telescope (LAT; Atwood et al. 2009) data using their analysis pipeline. Crocker et al. (2022) find the emitted Sgr gamma-ray distribution spatially traces the stellar distribution of Sgr. The spectral distribution of Sgr gamma-ray photons detected by Crocker et al. (2022) strongly favour millisecond pulsar (hereafter MSP) gamma-ray emission due to a combination of inverse Compton scattering of cosmic microwave background photons by high-energy electron–positron pairs escaping from the Sgr MSP population and magnetospheric MSP gamma-ray emission. Additionally, the H.E.S.S. collaboration (marginally) detected Sgr with a $2.05\,\sigma$ significance (Abramowski et al. 2014); however, they conclude that the results are 'well compatible' with a Gaussian significance distribution centred on zero. Viana et al. (2012) also analyse Sgr for sources of potential gamma-ray emission detectable with Cherenkov telescopes, concluding that predicted gamma-ray emission from millisecond pulsars outshines the prospective gamma-ray signal due to dark matter annihilation by several orders of magnitude.

This study seeks to predict the spatial and quantitative properties of the J-factor distribution of Sgr, providing a template for further searches for annihilation products from diverse particle physics models. In contrast to past studies utilizing stellar tracers to estimate the Sgr dark matter density distribution and J-factor (Viana et al. 2012; Evans et al. 2023), we derive the J-factor distribution for Sgr from the hydrodynamic simulation of Tepper-García & Bland-Hawthorn (2018). This allows more accurate modelling of the considerable changes to the Sgr internal dynamics, DM density distribution, and stellar density profile during the satellite's infall and tidal disruption (Kazantzidis et al. 2011; Newberg & Carlin 2016, ch. 2). Section 2.1 provides more information about these simulations, whilst the preliminary translation applied to the simulated particle distributions is detailed in Section 2.2. This translation does not change the resulting J-factor distribution magnitude. In Section 2.3, we adapt the methodology of Stoehr et al. (2003) and Charbonnier et al. (2011), utilizing the simulated Sgr dark matter particle mass and density values to produce a spatial J-factor flux distribution for use in indirect dark matter searches. The estimated volume-integrated J-factor value for Sgr is presented in Section 3.1, with further details of the spatial J-factor distribution of Sgr presented in Section 3.2. We then explore the implications of the J-factor value we derive in Section 4, before concluding in Section 5.

To further inform observational searches, we also produce profiles of the simulated stellar density and dark matter density squared in Section 3.3. The former distribution provides an indication of the expected gamma-ray emission from stellar-associated sources (for example millisecond pulsars) whilst the latter illustrates the

DM density profile and the absolute magnitude of the Sgr J-factor distribution.

## 2 METHODOLOGY

2.1 Simulation overview

Numerous simulations of the infall and tidal disruption of the progenitor galaxy of Sgr have been performed (e.g. Law et al. 2004; Law & Majewski 2010; Łokas et al. 2010; Dierickx & Loeb 2017), differing in the initial position, mass, and velocity of the Sgr progenitor and differing in the distribution of stellar and dark matter components. These differences in initial parameters have been shown to produce marked variations in the inferred orbit and evolution of the Sgr remnant (Jiang & Binney 2000; Law & Majewski 2010; Łokas et al. 2010).

In contrast to prior simulations, the simulation of Tepper-García & Bland-Hawthorn (2018) included a comprehensive treatment of gas in the Sgr progenitor. Realistic treatment of this gaseous component was shown to have a considerable effect on the orbital decay of Sgr, and also successfully reproduced other key features of the Sagittarius Dwarf/Stream system such as the approximate final position of stellar particles and the approximate angular size of the final Sagittarius Dwarf. Furthermore, in contrast to most previous simulations, this simulation includes initial conditions placing the Sgr progenitor at the virial radius of the Milky Way, which facilitates a more accurate treatment of the tidal disruption process during infall (Dierickx & Loeb 2017). This produced a more realistic evolution, including tidal stripping, of the Sgr Progenitor dark matter and stellar particles than simulations where the dwarf is artificially stripped and placed within the virial radius of the Milky Way.

Here, we exploit this simulation to produce an estimation of the expected dark matter distribution of Sgr. As detailed in Tepper-García & Bland-Hawthorn (2018), this simulation included a Sagittarius Dwarf progenitor of total mass 11×10^9 M$_\odot$ modelled with three live components. These components were a collisionless dark matter sub-halo of total mass $M_{\rm DM} = 10^{10}$ M$_\odot$ (with a mass per particle of 10^5 M$_\odot$), a collisionless stellar bulge of mass $M_{\rm S} = 4 \times 10^8$ M$_\odot$ (with a mass per particle of 4×10^3 M$_\odot$), and a gaseous halo of mass $M_{\rm G} = 6 \times 10^8$ M$_\odot$ (and a mass per particle of 6×10^3 M$_\odot$). Each of these components consisted of 10^5 particles, with the initial mass distribution of these three components governed by a spherical Hernquist profile (Hernquist 1990). The Milky Way was also modelled as a live system, of total mass 1.087×10^{12} M$_\odot$, with five components (collisionless DM halo, collisionless stellar disc, collisionless stellar bulge, gas corona, and gas disc) as detailed in table 1 of Tepper-García & Bland-Hawthorn (2018).

The simulation was run utilizing the version 3.0 of the Adaptive Mesh Refinement (AMR) scheme RAMSES (Teyssier 2002). The Sgr progenitor was placed at an initial location of $\vec{r}_0 = (125, 0, 0)$ kpc relative to the initial centre of the simulated Milky Way halo and had an initial velocity of $\vec{v}_0 \sim (-10, 0, 70)$ km s^{-1}. These initial conditions were adopted from the simulation of Dierickx & Loeb (2017), where they resulted in the closet match (in the present-day configuration) between six simulated Sgr phase-space coordinates and the observed properties of Sgr, whilst also resulting in agreement between the simulated and observed position of the Sagittarius Stream stellar debris. The infall of the Sgr progenitor was simulated in infall for a total duration of 3.6 Gyr, undertaking three pericentric passages, with the simulated stellar particles showing strong agreement with the observed distribution of Sagittarius Stream debris Tepper-García & Bland-Hawthorn (2018). For further details

---

[1] $(l_{\rm Sgr}, b_{\rm Sgr}) \approx (6°, -14°)$; Majewski et al. (2003).
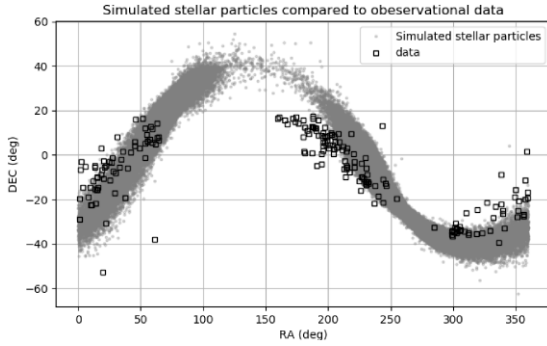
Figure 1. The simulated stellar particle population and observed stars (Majewski et al. 2003; Law, Johnston & Majewski 2005) in the Sagittarius Stream, reproduced from fig. 2 of Tepper-García & Bland-Hawthorn (2018).

of the simulation, including details of the AMR implementation, sub-grid physics, and a detailed description of the orbital evolution of the Sgr progenitor, see Tepper-García & Bland-Hawthorn (2018). For an extensive justification of the adopted initial conditions of the Sgr progenitor, see Dierickx & Loeb (2017).

2.2 Translation of the simulated Sagittarius Stream

However, despite the successes of the Tepper-García & Bland-Hawthorn (2018) model, it, in common with all previous simulations, fails to exactly reproduce the observed distribution of the Sagittarius Dwarf stars or the observed position of the Sgr Dwarf in the present day (Majewski et al. 2003; Belokurov et al. 2013), cf. Fig. 1. The projected location of the simulated Sgr (at the present day), defined as the position of the greatest projected stellar number (and mass) density[2] occurred at approximately $(\alpha, \delta) \simeq (282.77, -35.23)°$. This differs slightly from the observed location of Sgr reported in Majewski et al. (2003), $(l_{Sgr}, b_{Sgr}) \approx (6°, -14°)$ or $(\alpha_{Sgr}, \delta_{Sgr}) \simeq (284, -30.5)°$.

An accurate density distribution of dark matter in the area of Sgr, informed by simulations, is of crucial importance to informing indirect dark matter searches. For spatial likelihood searches, the position of Sgr is also crucial. Accordingly, to produce a dark matter and stellar template concordant with the observed Sagittarius Dwarf position, the simulated stars and dark matter particles from Sgr in the simulation of Tepper-García & Bland-Hawthorn (2018) were translated in RA and DEC such that the position of maximum simulated stellar projected number (and mass) density of Sgr (in the centre of the simulated Sgr) was located at the observed location of Sgr detailed in Majewski et al. (2003). Specifically, this translated the simulated stellar and dark matter particle distributions by $(\Delta\alpha, \Delta\delta) = (1.23, 4.73)°$; the location of the simulated Sgr was moved from a projected location of $(\alpha, \delta) \simeq (282.77, -35.23)°$ to $(\alpha', \delta') \simeq (284, -30.5)°$. The heliocentric distance of Sgr remained unchanged at 25.3 kpc following this translation process. Note that this translation preserves the 3D structure of the simulated stream, given this translation preserves the relative position of all Sgr particles and does not result in a change in heliocentric distance to Sgr. Accordingly, any quantities calculated from the simulated particle distributions remain unchanged in magnitude as a result of this transformation. Fig. 2

---

[2]The location of Sgr reported in Tepper-García & Bland-Hawthorn (2018), $(\alpha, \delta) = (285, -36.6)°$, is defined utilizing the position of maximum 3D mass density.
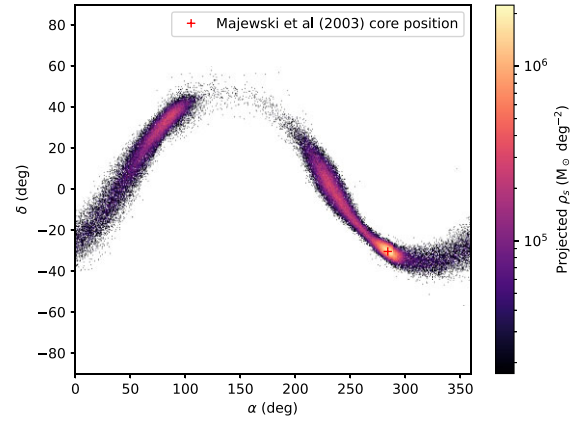
Figure 2. The translated projected mass density distribution of Sagittarius Stream simulated stellar particles. The position of these particles have been uniformly translated by $(\Delta\alpha, \Delta\delta) = (1.23, 4.73)°$ from their location in Tepper-García & Bland-Hawthorn (2018), and the projected location of the simulated Sgr is now $(\alpha, \delta) \simeq (284, -30.5)$. This is the location of Sgr reported by Majewski et al. (2003), as indicated by the red cross. As detailed in Section 2.2, this does not change the value of any projected quantities derived from the simulated particles.

illustrates the translated, projected simulated stellar mass density distribution. The projected mass density for each pixel was defined as the sum of particle masses divided by the angular area of the pixel:

$$\rho_s = \frac{1}{\alpha^2} \sum_i m_i, \tag{1}$$

where m_i is the mass of particle i and α is the angular width of the pixels. A constant square pixel side length of $\alpha = 0.458°$ was adopted for when calculating all projected distributions, which corresponds to a physical size of 0.0035 kpc at the distance of the Sagittarius Dwarf (25.3 kpc). This corresponds to a square pixel size of $\alpha^2 = 0.21$ deg^2. This square pixel size was adopted to facilitate use of these distributions in a maximum-likelihood analysis of Fermi-LAT data as the angular resolution of the Fermi-LAT instrument at 1 GeV is approximately equal to this adopted pixel size.

We used the translated projected dark matter particle distribution to calculate the Sgr J-factor distribution from the resulting projected Sagittarius Dwarf density profile. These calculations (detailed in Section 2.3) followed the method of Stoehr et al. (2003) to calculate the relevant distribution directly from simulated particle properties (also see Kuhlen ; Charbonnier et al. 2011).

2.3 Production of projected J-factor distributions

The self-annihilation or decay of several families of particle dark matter candidates is generically expected to produce gamma-ray emission (e.g. Bertone, Hooper & Silk 2005). In the case of WIMPs (Jungman, Kamionkowski & Griest 1996), primary and secondary gamma-rays are produced as products of self annihilation through multiple production channels (in addition to other annihilation products), with the volumetric annihilation rate scaling with the square of mass density. For astrophysical targets such as dwarf spheroidal galaxies and the Galactic centre the expected gamma-ray flux from WIMP self-annihilation, as a function of energy E per unit energy per solid angle Ω, can be modelled using an equation of
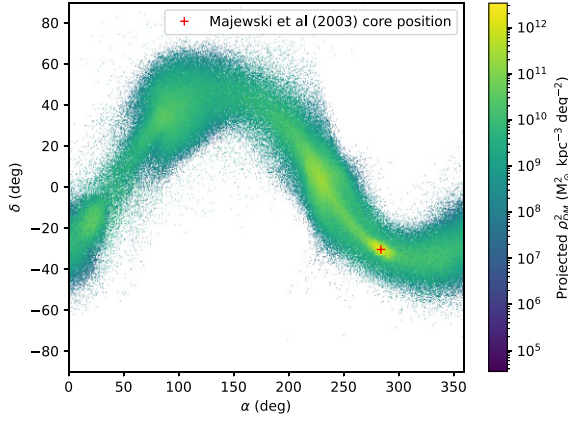
Figure 3. The projected ρ_{DM}^2 distribution of the translated Sagittarius Stream. As per the simulated stellar translation, all particles are translated by $(\Delta\alpha, \Delta\delta) = (1.23, 4.73)°$ from their detailed location in Tepper-García & Bland-Hawthorn (2018). As detailed in Section 2.2, this does not change the value of any projected quantities derived from the simulated particles. The observed location of Sgr reported in Majewski et al. (2003) is indicated with a red cross, which is coincident with the translated simulated Sgr dark matter population.

the form (Charbonnier et al. 2011):

$$\frac{d\Phi_\gamma}{dE_\gamma}(E, \Delta\Omega) = \frac{1}{4\pi}\frac{\langle\sigma v\rangle}{2m^2}\frac{dN_\gamma}{dE_\gamma}(E) \times J(\Delta\Omega), \quad (2)$$

where the velocity averaged DM annihilation cross-section $\langle\sigma v\rangle$, DM particle mass m, and spectral energy distribution of emitted gamma-rays $\frac{dN_\gamma}{dE}(E)$ are model-dependent parameters. Together, these terms detail the spectral distribution of the gamma-ray annihilation products. In contrast, the 'J-factor' $J(\Delta\Omega)$ specifies the spatial dependence of the gamma-ray flux. Explicitly in the case of WIMP annihilation (Charbonnier et al. 2011),

$$J = \int_{\Delta\Omega}\frac{dJ}{d\Omega} = \int_{\Delta\Omega}\int\rho^2(r, \Omega)dr\,d\Omega \quad (3)$$

where ρ is the density distribution of dark matter along the line of sight radii r to the object of angular size $\Delta\Omega$.

However, accurately constraining the J-factor value for the dark matter component of Sgr is difficult due to ongoing tidal disruption (and uncertain foreground/background gamma-ray sources). This results in a dark matter density distribution subject to significant uncertainties, comparatively difficult (compared to classical dSph systems) to constrain with stellar tracers. Simulations are often used to model the dark matter density distribution of Sgr; however, to the knowledge of the authors no simulation has been utilized to model the J-factor distribution and compute an integrated J-factor value for Sgr.

The quantity ρ_{DM}^2, the dark matter spatial density squared integrated over a given volume, was estimated directly from the simulation output particle density ρ_i in accordance with the equation (Stoehr et al. 2003):

$$\rho_{DM}^2 = \int_V\rho_{DM}^2\,dV = \sum_i\rho_i m_i, \quad (4)$$

where m_i is the (constant) simulated particle mass. The projected distribution of this quantity for the Sagittarius Stream is shown in Fig. 3, calculated for each pixel by summing over all particles in the pixel in accordance with equation (4) before division by the pixel size ($\alpha^2 = 0.21$ deg^2). Note that whilst Stoehr et al. (2003) utilize equation (4) to calculate the J-factor value for a given volume element, in this
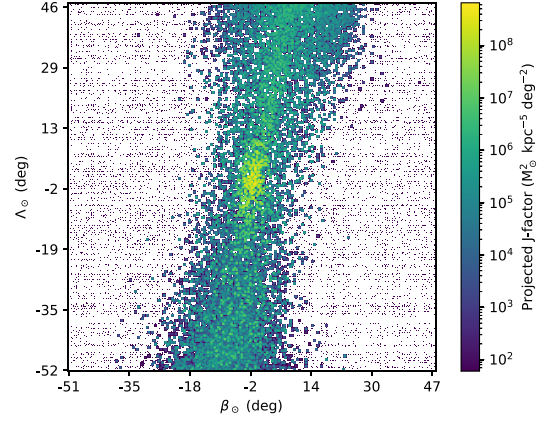
Figure 4. The projected J-factor distribution centred on the location of the simulated Sagittarius Dwarf, depicted in the coordinate system of Belokurov et al. (2013). The pixel size adopted in this figure is $\alpha^2 = 0.21$ deg^2. The location of Sgr in this coordinate system is $(\beta_{Sgr}, \Lambda_{Sgr}) = (-1.48, -0.22)°$.

study J-factor values for substructures within the simulation were calculated including an inverse-square distance dependence given the extended nature of Sgr. Specifically, we include a factor of $1/(4\pi r_i^2)$ for each particle i to account for the size of the flux sphere for each simulation particle. With this distance dependence, the J-factor definition adopted in this study is equivalent to a flux, not absolute brightness. The contribution of each particle i to the J-factor value for each volume element V_b at a heliocentric distance r of the considered structure was thus calculated as:

$$J_b = \int_{V_b}\rho_{DM}^2/\left(4\pi r^2\right)\,dV = \sum_i\rho_i m_i/\left(4\pi r_i^2\right), \quad (5)$$

where ρ_i is the dark matter density, m_i is the mass of particle i and r_i is the distance from the Sun to particle i. As shown in Appendix A, this definition is equivalent to the J-factor definition provided by Charbonnier et al. (2011), though differs by a factor of 4π due to the flux sphere surface area normalization factor. The total summed J-factor value for an extended substructure (for example Sgr) was calculated by summing over the constituent volume elements V_b:

$$J = \Sigma_b\int_{V_b}\rho_{DM}^2/\left(4\pi r^2\right)\,dV = \Sigma_b\Sigma_i\rho_i m_i/\left(4\pi r_i^2\right)$$
$$= \Sigma_{i'}\rho_{i'}m_{i'}/\left(4\pi r_{i'}^2\right) \quad (6)$$

for all particles i' in the extended substructure (potentially of multiple volume elements).

For the analysis of this study, projected distributions of the line-of-sight integrated J-factor values were produced using the HEALPix pixelization scheme (Górski et al. 2005) to sum the particle values in spatial pixels (volume elements). The integrated J-factor value for each pixel was calculated using equation (5) and converted into a projected value through division by the pixel size. The side width of the square bins adopted in this plot, and in all 2D plots in this paper, was $\alpha = 0.458°$, which corresponds to a square pixel area of $\alpha^2 = 0.21$ deg^2. As aforementioned, this square pixel size corresponds to the resolution of the Fermi-LAT instrument at 1 GeV and was chosen to allow the use of these projected distributions in analyses of Fermi-LAT data. Fig. 4 illustrates the projected dark matter J-factor distribution at the location of the Sagittarius core in the units of M$_\odot^2$ kpc^{-5} deg^{-2}. In Fig. B1, this distribution is also shown in the physical units of M$_\odot^2$ kpc^{-7}, converted from the units of M$_\odot^2$ kpc^{-5}

deg^{-2} through division of each pixel b by the factor C_b:

$$C_b = \left(2\tan(\alpha/2) \times \bar{d}_b\right)^2 / \alpha^2, \tag{7}$$

where $\alpha = 0.458°$ was the constant angular width of each pixel and $\bar{d}_b$ was the mean particle distance in the given pixel b. We have verified that the standard deviation of C_b for each pixel remains significantly below the value of C_b, and accordingly that the transformation is robust to the variance of particle distances about the mean. In these figures, we use the $(\beta_\odot, \Lambda_\odot)$ coordinate system of Belokurov et al. (2013), which is a variant of the coordinate system utilized in Majewski et al. (2003). In the system of Belokurov et al. (2013), the $\Lambda_\odot$ axis proceeds along the Sagittarius Stream in the direction of motion of Sgr, whilst the $\beta_\odot$ axis points toward the North Galactic Pole. These figures detail the region $\Lambda_\odot \in [\Lambda_0 \pm 50°]$, $\beta_\odot \in [\beta_0 \pm 50°]$, where $(\beta_0, \Lambda_0) = (-1.48, -2.22)$. Sgr is located at $(\beta_{\mathrm{Sgr}}, \Lambda_{\mathrm{Sgr}}) = (-1.48, -0.22)°$ in this coordinate system.

In addition to this paper analysing the J-factor distribution of Sgr, an upcoming study (Venville et al., *in preparation*, hereafter Paper II) will discuss the all-sky J-factor distribution of the Sagittarius Stream and investigate the possibility of detecting gamma-ray emission from the Sagittarius Stream utilizing Fermi LAT data.

3 RESULTS: PREDICTED DARK MATTER DENSITY AND J-FACTOR DISTRIBUTIONS FROM THE SAGITTARIUS DWARF

3.1 Predicted J-factor magnitude of the Sagittarius Dwarf

In accordance with equation (6), the integrated J-factor value for Sgr was calculated by summing all particle values along the line of sight and within the projected 'core radius' (corresponding to the approximate bound radius) of $\alpha_{\mathrm{Sgr}} \simeq 3.7°$ (Majewski et al. 2003) of the centre of the simulated Sagittarius Dwarf, defined as $(\alpha, \delta) \simeq (284, -30.5)°$ in Section 2.2 and Majewski et al. (2003). This radius corresponds to a physical size of 1.6 kpc at the location of Sgr and a conical integration region of solid angle of $\Omega_{\mathrm{Sgr}} \simeq 3.6 \times 10^{-3}$ sr.

This integrated J-factor value of Sgr was 1.48×10^{10} M$_\odot^2$ kpc^{-5}. Note that this is not a projected J-factor value but (in accordance with equation 6) instead corresponds to a three-dimensional volume summation of the particle J-factor values within this conical integration region. It should also be noted that due to the archival nature of the utilized simulation, the convergence of the derived Sgr particle density profile at varying resolutions cannot be studied. As increasing resolution *could* result in an increasing Sgr central density and correspondingly increased J-factor values at small radii, the J-factor value derived in this study is a conservative lower limit.

Prior determinations of the J-factor value for Sgr are consistently higher than value derived in this paper. Abramowski et al. (2014) estimate a J-factor value of $J_{\mathrm{Sgr}} = 2.88 \times 10^{12}$ M$_\odot^2$ kpc^{-5} integrated across a solid angle of $\Delta\Omega = 10^{-5}$ sr $\simeq 0.032$ deg^2, whereas Viana et al. (2012) calculate a J-factor value of $J_{\mathrm{Sgr}} = 1.5 \times 10^{15}$ M$_\odot^2$ kpc^{-5} for an integration solid angle of $\Delta\Omega = 2 \times 10^{-5}$ sr $= 0.07$ deg^2. These results shall be discussed in Section 4.

The projected J-factor distribution for Sgr produced in this study was fitted (in conjunction with the additional templates described in Crocker et al. 2022 to Fermi-LAT gamma-ray data utilizing the exact methodology detailed in Crocker et al. 2022). The normalized DM J-factor distribution was detected with a maximum significance of $<1\sigma$, including during evaluation of transitional and rotational tests.

This DM template is thus significantly less favoured by the data than templates tracing the Sgr projected stellar density distribution (detected with an 8.1 σ significance). Therefore, Crocker et al. (2022) concluding that MSPs are the likely cause of gamma-ray emission from the direction of Sgr is consistent both with the findings of Viana et al. (2012) and the predicted J-factor distribution for Sgr calculated in this study. To provide further support for this conclusion, we utilize the J-factor value calculated here and the gamma-ray photon flux attributed to Sgr in Crocker et al. (2022) to calculate a lower limit on the required WIMP cross-section $\langle\sigma v\rangle$ to produce this gamma-ray photon flux. In accordance with equation (2) and Mazziotta et al. (2012), the photon flux Φ_γ can be expressed as

$$\Phi_\gamma(E, \Delta\Omega) = J(\Delta\Omega) \times \frac{1}{2} \frac{\langle\sigma v\rangle}{4\pi m_\chi^2} \Sigma_f N_f(E, m_\chi) B_f, \tag{8}$$

where m_χ is the mass of the WIMP and $N_f(E, m_\chi)$ is the differential photon spectrum produced by pair annihilation into a final state f with a branching fraction B_f. Setting $N_f = B_f = 1$ allows the calculation of a lower limit on the cross-section value for an assumed WIMP mass and J-factor value $J(\Delta\Omega)$. For the J-factor of magnitude $J_{\mathrm{Sgr}} \sim 10^{10}$ M$_\odot^2$ kpc^{-5} as determined in this study, the lower limit on the cross-section required to produce the GeV-band gamma-ray number flux $\Phi_\gamma \sim 10^{-8}$ cm^{-2} s^{-1} observed in Crocker et al. (2022) is $\langle\sigma v\rangle \sim 6 \times 10^{-20}$ cm^3 s$^{-1} \left(\frac{m_\chi}{100\,\mathrm{GeV}}\right)^2$. Such a velocity averaged cross-section is inconsistent with existing constraints on WIMP cross-sections (Abazajian et al. 2020, fig. 1; Albert et al. 2017, fig. 10, left). For example, assuming a WIMP mass of 10 GeV, the lower limit on the required cross-section implied by our study is $\langle\sigma v\rangle \sim 6 \times 10^{-24}$ cm^3 s^{-1}, far in excess of the upper limit of $\langle\sigma v\rangle \sim 3 \times 10^{-27}$ cm^3 s^{-1} derived from analysis of other measured dSph galaxy J-factors (Albert et al. 2017, fig. 10, left). It also significantly exceeds the upper limit of $\langle\sigma v\rangle \sim 3 \times 10^{-28}$ cm^3 s^{-1} derived from analysis of the Galactic Centre Excess (whilst assuming a Navarro–Frenk–White (NFW) DM density distribution) detailed in Abazajian et al. (2020, fig. 1). Similarly, for a WIMP mass of 100 GeV, the lower limit of $\langle\sigma v\rangle \sim 6 \times 10^{-20}$ cm^3 s^{-1} implied by this study far exceeds the upper limits of $\langle\sigma v\rangle \sim 1.5 \times 10^{-26}$ cm^3 s^{-1}, derived from analysis of other measured dSph galaxy J-factors in Albert et al. (2017), and $\langle\sigma v\rangle \sim 2 \times 10^{-27}$ cm^3 s^{-1}, derived from analysis of the Galactic Centre Excess in Abazajian et al. (2020). This incompatibility of the implied WIMP DM velocity averaged cross-section found by this study with existing constraints reinforces the conclusions of Crocker et al. (2022) and strongly disfavours WIMP DM as the source of the observed gamma-ray emission from the Sgr.

3.2 1D J-factor profiles

As the J-factor value for Sgr in this study is low compared to prior estimations (Viana et al. 2012; Abramowski et al. 2014) and significant gamma-ray emission from MSPs is present at the location of Sgr (Crocker et al. 2022), morphological features of the Sgr J-factor distribution may aid detection of any gamma-ray emission due to DM annihilation. Thus, the following section shall detail morphological characteristics of the DM J-factor distribution inferred from the simulations. This has the potential advantage, compared to DM distributions derived from stellar distribution data (e.g. Viana et al. 2012), of more accurate treatment of the tidal disruption of the DM component and avoiding the need to assume dynamical equilibrium or spherical symmetry in the DM (or stellar tracer) population.
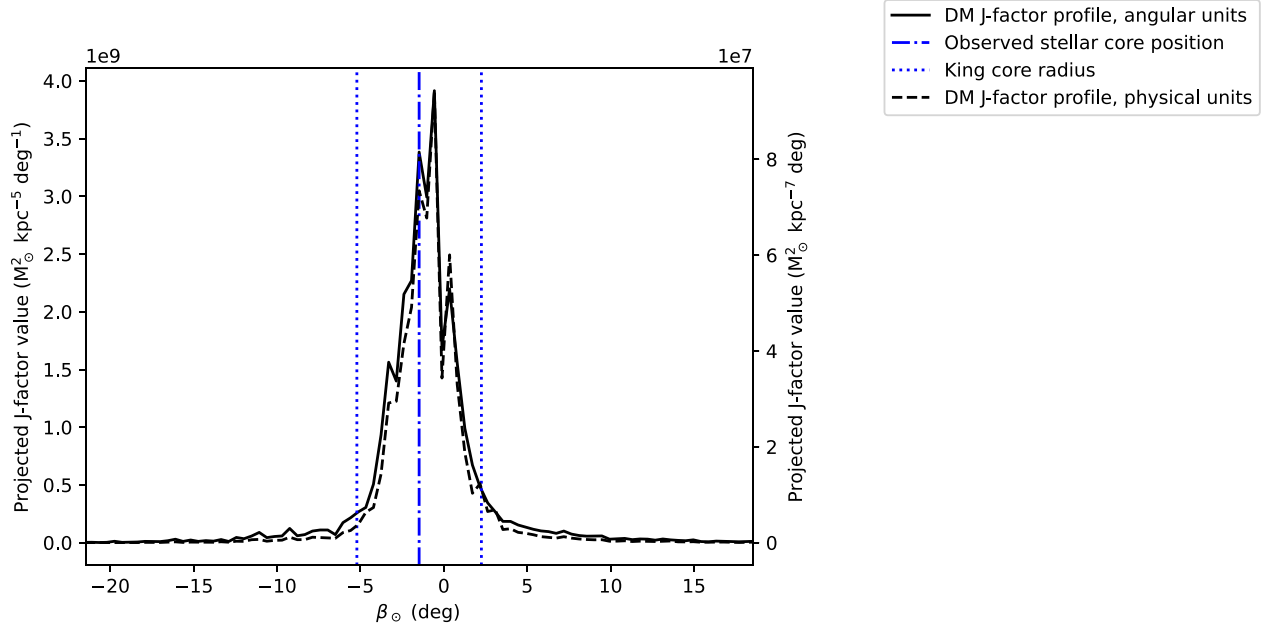
Figure 5. The projected J-factor profile for the dark matter particles as a function of $\beta_\odot$, within the region of interest defined in Section 2.3 and depicted in Fig. 4. The adopted $\beta_\odot$ bin size is $0.458°$. This region of interest spans the range $-50° < \Lambda_\odot < 50°$. Note that this J-factor profile is depicted in both the angular units of $M_\odot^2 \, \mathrm{kpc}^{-5} \, \mathrm{deg}^{-2}$ (derived from the distribution depicted in Fig. 4) and the physical units of $M_\odot^2 \, \mathrm{kpc}^{-7}$ (derived from the distribution depicted in Fig. B1).
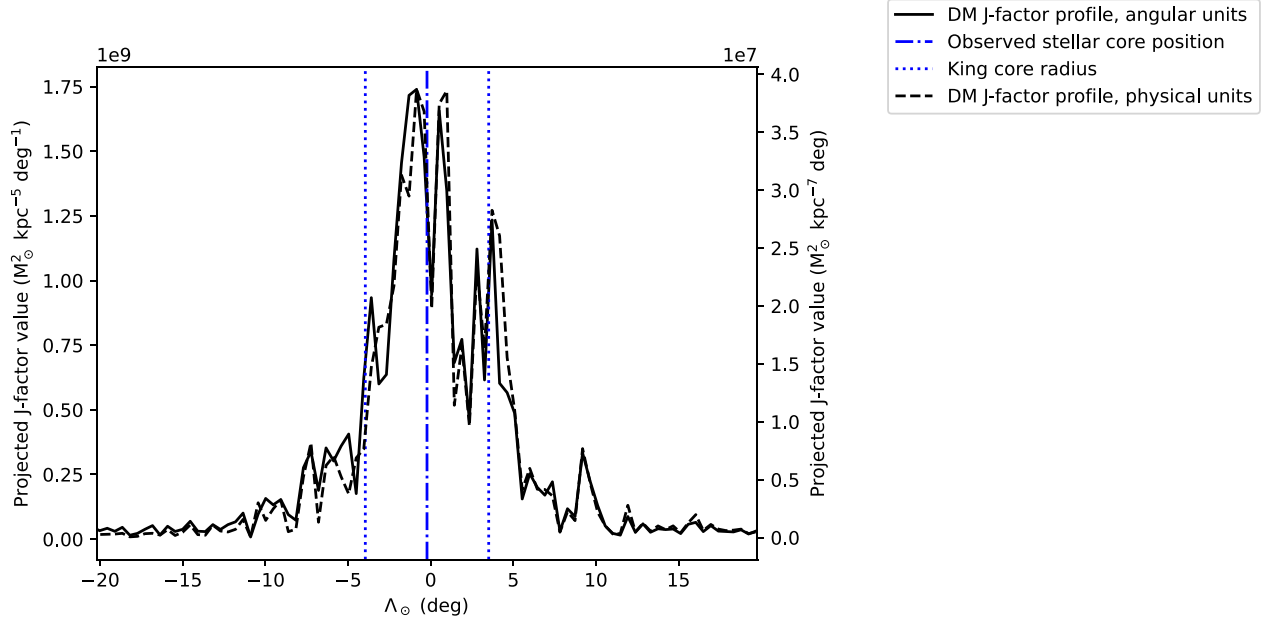
Figure 6. The projected J-factor profile for the dark matter particles as a function of $\Lambda_\odot$, within the region of interest defined in Section 3.2. This region of interest spans the range $-50° < \beta_\odot < 50°$. The adopted $\Lambda_\odot$ bin size is $0.458°$. As per the J-factor profile as a function of $\beta_\odot$ depicted in Fig. 5, the J-factor profile is depicted in both the angular units of $M_\odot^2 \, \mathrm{kpc}^{-5} \, \mathrm{deg}^{-2}$ (derived from the distribution depicted in Fig. 4) and the physical units of $M_\odot^2 \, \mathrm{kpc}^{-7}$ (derived from the distribution depicted in Fig. B1).

The projected J-factor distribution summed in bins of $\beta_\odot$ over the region of interest detailed in Section 2.3 is illustrated in Fig. 5. The bin width adopted for this binning, and all subsequent 1 dimensional profiles in this paper, was $0.458°$. This bin width is equal to the angular resolution of the Fermi-LAT instrument at

1 GeV. It is an intentionally identical width to the width/length of the square pixels utilized in calculating the projected J-factor distributions detailed in Section 2.3; as aforementioned, the square pixel size of these projected distributions was chosen to allow use of these distributions in a maximum-likelihood analysis of Fermi-

LAT data. As is evident in Fig. 5, there is a marked increase in the magnitude of the predicted J-factor at the location of Sgr; however, gamma-ray emission from stellar populations or millisecond pulsars are also expected to increase in magnitude at this location (Viana et al. 2012).

The magnitude of the projected J-factor profile depicted as a function of $\beta_\odot$ in Fig. 5 at the observed location of Sgr is 3.4×10^9 $M_\odot^2$ kpc^{-5} deg^{-1}; this is approximately 13 times the J-factor value of 2.6×10^8 $M_\odot^2$ kpc^{-5} deg^{-1} at the core radius of Sgr in the negative $\beta_\odot$ direction, namely $(\beta_\odot, \Lambda_\odot) = (-5.21, 0)°$. At the core radius of Sgr, but in the positive $\beta_\odot$ direction, the J-factor value is 4.6×10^8 $M_\odot^2$ kpc^{-7} deg, a factor of approximately 7.3 lower than the J-factor value at the observed location of Sgr. The difference between these values indicates the relative J-factor contrast between the core and outskirts of Sgr. This contrast is significantly lower than the stellar number density contrast across similar angular scales in the fitted templates adopted in Crocker et al. (2022, supplementary fig. 1). Accordingly, the DM J-factor templates are likely insufficiently peaked to fit the spatial gamma-ray emission distribution observed for Sgr.

Similarly, the projected J-factor profile for the DM particles summed in bins of $\Lambda_\odot$ is illustrated in Fig. 6. The value of this distribution at the observed core central position is 1.3×10^9 $M_\odot^2$ kpc^{-5} deg^{-1}, whilst the J-factor value at the core radius in negative $\Lambda_\odot$ direction $(\beta_\odot, \Lambda_\odot) = (0, -4.0)°$ is 6.9×10^8 $M_\odot^2$ kpc^{-5} deg^{-1}. The J-factor value at the core radius in the positive $\Lambda_\odot$ direction, at $(\beta_\odot, \Lambda_\odot) = (0, 3.51)°$, is 9.5×10^8 $M_\odot^2$ kpc^{-5} deg^{-1}. However, the $\Lambda_\odot$ profile detailed in Fig. 6 shows significant asymmetry and variance on small angular scales, resulting from the tidal disruption of the Sgr halo. Regardless, this J-factor profile is also likely insufficiently peaked to fit the spatial gamma-ray distribution attributed to Sgr in Crocker et al. (2022).

To compare the width of the 1D projected J-factor profiles to observed stellar distributions and simulated DM/stellar density distributions (see Section 3.3), distribution functions were fitted to scaled versions of the projected J-factor profiles with a maximum value of 1.0, as illustrated in Fig. C1 for the dark matter J-factor $\beta_\odot$ profile and Fig. C2 for the $\Lambda_\odot$ profile. We choose to scale the profiles with angular units to avoid any small-scale variation caused on the profiles with physical units by variation in the applied divisor C_b between pixels. The selected form of these functions, either a Voigt, Moffat, Gaussian or Gaussian with constant vertical offset, were selected by minimizing the following non-linear least squares optimization function value O:

$$O = \sum_x \left(y'(x) - y(x) \right)^2, \tag{9}$$

where y' is the value of the fitted function and y is the value of the 1D profile at a given value of $x = \beta_\odot$ or $x = \Lambda_\odot$, depending on the 1D profile in question. These functions were fitted to the 1D J-factor profiles using a Levenberng–Marquardat (Levenberg 1944; Marquardt 1963) non-linear least squares algorithm, as implemented in ASTROPY[3] (Astropy Collaboration 2013, 2018, 2022, in the case of the Moffat, Gaussian or Voigt functions) or SCIPY[4] (Virtanen et al. 2020, in the case of the offset Gaussian function). A Moffat function of the form

$$f(x) = A \left(1 + \frac{(x - x_0)^2}{\gamma^2} \right)^{-\alpha} \tag{10}$$

best fit both the scaled $\beta_\odot$ and scaled $\Lambda_\odot$ J-factor profiles as it more accurately models the wide tails of these distributions resulting from the tidal disruption of Sgr. The parameters of these fits are detailed in Table 1. The full width at half-maximum (FWHM) of the Moffat function fitted to the scaled J-factor profile along the $\beta_\odot$ axis is $3.7°$, comparable to the observed 'core radius' of Sgr reported in Majewski et al. (2003). The FWHM of the Moffat function fitted to the scaled DM $\Lambda_\odot$ J-factor profile is $4.9°$. This illustrates the known tidal disruption of Sgr along the $\Lambda_\odot$ axis (Majewski et al. 2003; Łokas et al. 2010). The Sgr J-factor distribution is thus notably extended along both $\beta_\odot$ and $\Lambda_\odot$ axes, providing a valuable morphological discriminant to point-like sources of emission present in analysis procedures given any gamma-ray emission from the Sgr DM population would follow a similarly extended distribution.

We also conduct an estimation of the percentage contribution of any small-scale profile irregularities in the 1D projected J-factor profiles to the overall J-factor value. To compute this contribution, we compute a J-factor value by integrating the fitted 1D distributions over a given interval, and compare this to the J-factor values found by numerically integrating the 1D projected profile bins over the same interval. This numerical integral utilized the cumulative trapezoid method, as implemented in the SCIPY (Virtanen et al. 2020) function SCIPY.INTEGRATE.CUMULATIVE_TRAPEZOID(). This allows us to estimate the deviation of the simulated J-factor value calculated over the given interval from the fitted smoothed profile, thus estimating the contribution of any small-scale profile irregularities in the J-factor profiles to the simulated J-factor value. This is important to calculate given the simulation could cause spurious substructure in the 1D profiles. However, the significant tidal disruption of Sgr also could cause substructure not accurately modelled by conventional smooth profiles. Over a range $-20° < \beta_\odot < 20°$, the percentage difference between the total integrated J-factor value of the scaled $\beta_\odot$ J-factor profile and the integrated value of the fitted Moffat distribution (both depicted in Fig. C1) was calculated as 1.34 per cent. Similarly, the percentage difference in integrated J-factor values between the scaled $\Lambda_\odot$ J-factor profile and fitted Moffat distribution (depicted in Fig. C2) was calculated as 3.0 per cent over the range $-20° < \Lambda_\odot < 20°$. These values imply a similarly low contribution from small-scale J-factor distribution variance within these intervals to the J-factor values reported in this study, in spite of the marked small-scale variation exhibited by these profiles.

As is evident in Figs 5 and 6, whilst a point source approximation for the J-factor distribution of Sgr is clearly invalid, the J-factor distribution is highly concentrated with a significant fraction of the total emission situated within the core radius $\alpha_{\rm Sgr} \simeq 3.7°$ of Sgr reported in Majewski et al. (2003). Figs 7 and 8 show the cumulative summed J-factor value as a function of $|\beta_\odot|$ and $|\Lambda_\odot|$, respectively, calculated by summing the individual particle J-factor values (in accordance with equation 6) within the given angular distance r from the centre of the simulated Sgr halo. Note that when summing along each axis (for example $\beta_\odot$), the summation range along the alternate axis (for example $\Lambda_\odot$) is unrestricted. Also shown are the angular distances along each axis containing 50 per cent and 90 per cent of the total summed J-factor value within $20°$ of the centre of the simulated Sgr halo. Along the $\beta_\odot$ axis, 50 per cent (90 per cent) of the total cumulative J-factor emission within $|\beta_\odot| = 20°$ occurs within an angular distance of $|\beta_\odot| = 1.7°$ ($|\beta_\odot| = 4.8°$), whilst some $\simeq 83$ per cent of the total cumulative J-factor emission is located within the Sgr core radius. Along the $\Lambda_\odot$ axis, the core radius of Sgr contains 62 per cent of the total cumulative J-factor emission within $|\Lambda_\odot| = 20°$; 90 per cent of the total J-factor emission within $|\Lambda_\odot| = 20°$ is located within an angular distance of $|\Lambda_\odot| = 8.6°$.

---

[3]The fitting function implemented in ASTROPY is detailed at this website.
[4]The fitting function implemented in SCIPY is detailed at this website.

Table 1. The parameters of the distribution functions fitted to scaled 1D projected J-factor, simulated stellar density (ρ_s) and DM density squared (ρ_{DM}^2) distributions. These functions were fitted to provide insight into the morphology of expected gamma-ray emission from DM annihilation (in the case of the J-factor distributions) and stellar-associated sources (in the case of the ρ_s distributions). The ρ_{DM}^2 distributions provide insight into the tidally disrupted Sgr DM halo. The scaled J-factor distributions and fitted functions are further discussed in Section 3.2, whilst the scaled ρ_s and ρ_{DM}^2 distributions and fitted functions are discussed in Section 3.3.
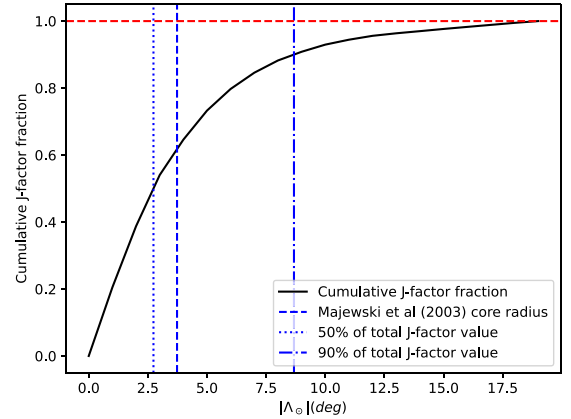
Profile	Fitted distribution	Fitted parameters	FWHM	Optimization function value
DM J-factor $-\beta_\odot$	Moffat	$A = 0.854$ $x_0 = -1.07$ $\gamma = 2.12$ $\alpha = 1.50$	3.7°	0.141
DM J-factor $-\Lambda_\odot$	Moffat	$A = 0.885$ $x_0 = -0.437$ $\gamma = 2.70$ $\alpha = 0.92$	4.9°	0.745
$\rho_s - \beta_\odot$	Moffat	$A = 0.941$ $x_0 = -0.757$ $\gamma = 2.70$ $\alpha = 1.06$	4.9°	0.181
$\rho_s - \Lambda_\odot$	offset Gaussian	$a = 8.65$ $mu = -0.390$ $\sigma = 5.10$ $c = 0.094$	13.6°	0.875
$\rho_{DM}^2 - \beta_\odot$	Moffat	$A = 0.873$ $x_0 = -1.04$ $\gamma = 1.57$ $\alpha = 0.978$	3.6°	0.145
$\rho_{DM}^2 - \Lambda_\odot$	offset Gaussian	$a = 5.62$ $mu = -0.196$ $\sigma = 3.07$ $c = 0.041$	8.0°	0.838
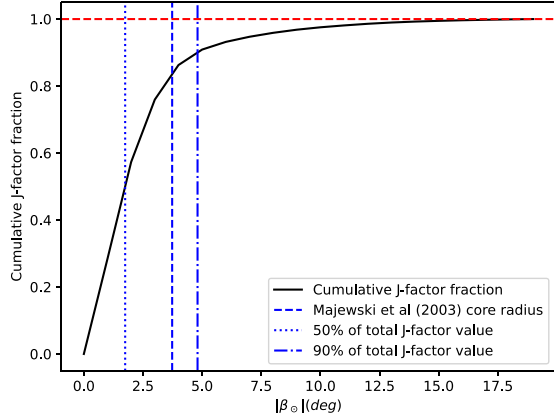
Figure 7. The cumulative J-factor fraction (within $|\beta_\odot| = 20°$) as a function of $|\beta_\odot|$. As discussed in Section 3.2, the core radius of Sgr reported in Majewski et al. (2003) contains 83 per cent of the cumulative J-factor emission.


Figure 8. The cumulative J-factor fraction (within $|\Lambda_\odot| = 20°$) as a function of $|\Lambda_\odot|$. As discussed in Section 3.2, the core radius of Sgr contains 62 per cent of the cumulative emission over this interval.

3.3 Projected ρ_s and ρ_{DM}^2 profiles

Given that explaining the observed gamma-ray emission from Sgr with the derived J-factor distribution is inconsistent with existing constraints on DM annihilation cross-sections, this section describes the distributions of simulated stellar density (ρ_s) and the square of DM density (ρ_{DM}^2) to further inform observational analyses of Sgr. The expected gamma-ray emission flux from stellar-associated sources is proportional to the projected stellar density Crocker et al. (2022), whilst the flux of gamma-ray emission from DM annihilation is proportional to the projected J-factor distribution (see Section 2.3). This section facilitates a comparison of the morphology of the expected emission from these two sources. However, it should be noted that the actual gamma-ray emission flux from these sources is highly dependent on the assumed gamma-ray emission
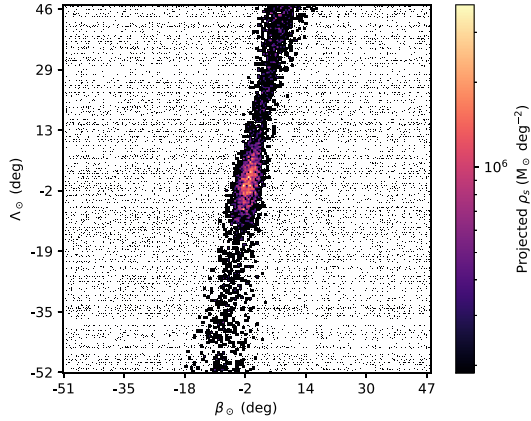
Figure 9. The projected ρ_s distribution for Sgr, depicted in the coordinate system of Belokurov et al. (2013), in the angular units of $M_\odot$ deg^{-2}. The adopted pixel size in this figure is $\alpha^2 = 0.21$ deg^2. The projected ρ_s peak is located at $(\beta_\odot, \Lambda_\odot) \simeq (-2.4, -0.9)^\circ$, an offset of approximately 1.4° from the projected dark matter ρ_{DM}^2 peak.
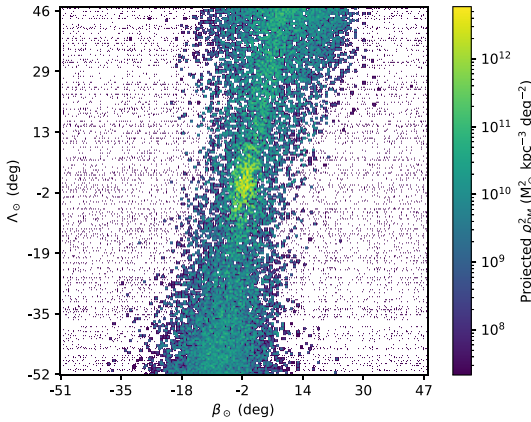
Figure 10. The projected ρ_{DM}^2 distribution for Sgr in the coordinate system of Belokurov et al. (2013), in the angular units of $M_\odot^2$ kpc^{-3} deg^{-2}. The adopted pixel size in this figure is $\alpha^2 = 0.21$ deg^2. The increased dark matter density within the core radius of Sgr is clearly visible, with the projected ρ_{DM}^2 peak located at $(\beta_\odot, \Lambda_\odot) \simeq (-1.0, -1.3)^\circ$.

model; accordingly, the relative magnitudes of the J-factor and ρ_s distributions do not provide an accurate indication of the primary dominant gamma-ray emission mechanism expected for Sgr.

Fig. 9 displays the projected ρ_s distribution at the location of the Sagittarius core, calculated for each pixel in accordance with equation (1) by dividing the sum of particle mass in the pixel by the pixel size ($\alpha^2 = 0.21$ deg^2). As per the 2D projected J-factor distributions discussed in Section 2.3, all figures in this section are depicted in the $(\beta_\odot, \Lambda_\odot)$ coordinate system of Belokurov et al. (2013) and were produced utilizing the HEALPix pixelization scheme Górski et al. (2005) to sum the relevant particle quantities in spatial pixels.

As discussed in Section 2.3, the Sgr ρ_{DM}^2 (and DM density) distribution is difficult to model with stellar tracers due to the ongoing tidal disruption of the Sgr halo. The ρ_{DM}^2 distribution also is equal to the absolute magnitude of the Sgr J-factor definition, as detailed in Section 2.3, which allows comparison to other studies of indirect dark matter annihilation utilizing absolute magnitude J-factor definitions

(e.g Stoehr et al. 2003). Accordingly, in this appendix we also present the projected Sgr ρ_{DM}^2 distribution to inform future studies attempting to calculate the DM density distribution or the J-factor distribution of Sgr. Fig. 10 shows this projected ρ_{DM}^2 distribution for Sgr. The displayed projected ρ_{DM}^2 value for each pixel was calculated by dividing the result of equation (4) for each pixel by the (constant) pixel size ($\alpha^2 = 0.21$ deg^2).

A quantity of potential interest to observational analyses of Sgr is the projected offset in maximum density between the simulated stellar and dark matter populations. To calculate this offset, the projected ρ_s^2 (not ρ_s) and ρ_{DM}^2 distributions were smoothed, such that the value of a pixel b in the smoothed distribution was the mean value of the density distribution in pixel b and the immediate eight surrounding pixels. This smoothing minimized the impact of small-scale density fluctuations on determining the position of maximum density, as did the use of the ρ_s^2 instead of the ρ_s distribution. The peak of the ρ_s distribution is necessarily coincident with the ρ_s^2 distribution peak.

The pixel corresponding to the projected maximum squared density was then located for both simulated stellar and dark matter populations. In the coordinate system of Belokurov et al. (2013), these pixels were located at $(\beta_\odot, \Lambda_\odot) = (-1.02, -1.31)^\circ$ and $(\beta_\odot, \Lambda_\odot) = (-2.40, -0.85)^\circ$ for the dark matter and simulated stellar particle populations, respectively (see Section 2.3 for a detailed explanation of this coordinate system). The projected offset between these pixel positions was thus 1.44°.

In their gamma-ray analysis employing an Sgr stellar template, Crocker et al. (2022) found moderate evidence (4.5σ statistical significance) for a shift in the best-fitting position of the template 180° away from the dwarf galaxy's travel direction ($\sim 4^\circ$ towards the Galactic south). This is evidence for an offset between the peak of the gamma-ray emission and the centre of Sgr defined by its stars. The much smaller offset, found here, between the simulated DM population and the simulated stellar population of Sgr does not seem to provide an explanation of the offset tentatively found by Crocker et al. (2022). Furthermore, the offset between the simulated stellar and dark matter density peaks we find is in the wrong direction to explain the offset found by Crocker et al. (2022). This in turn tentatively indicates that the observed gamma-ray emission is not due to gamma-ray emission from DM annihilation in Sgr, consistent with Crocker et al. (2022).

As aforementioned, comparative analysis of the J-factor and ρ_s distributions provides valuable information on the comparative morphology of the expected gamma-ray emission from DM annihilation and stellar-associated sources, whilst the ρ_{DM}^2 distribution provides valuable insight on the shape of the Sgr DM halo. Accordingly, following the methodology outlined in Section 3.2, we derived projected 1D ρ_s and ρ_{DM}^2 profiles from the 2D distributions respectively depicted in Figs 9 and 10, as functions of $\Lambda_\odot$ and $\beta_\odot$. These distributions were then scaled (such that their maximum value was 1.0) and fitted with distribution functions to measure their width and facilitate comparison to the 1D projected J-factor profiles discussed in Section 3.2. As per the 1D projected J-factor profiles discussed in Section 3.2, the choice of fitted function was selected by minimizing the non-linear least squares optimization detailed in equation (9). The functions were again fitted to the 1D profiles using a Levenberg–Marquardat (Levenberg 1944; Marquardt 1963) non-linear least squares algorithm implemented in ASTROPY (Astropy Collaboration 2013, 2018, 2022, in the case of the Moffat, Gaussian or Voigt functions) or SCIPY (Virtanen et al. 2020, in the case of the offset Gaussian function). The offset Gaussian function, which best fit the 1D projected ρ_s and ρ_{DM}^2 distributions as functions of $\Lambda_\odot$, is
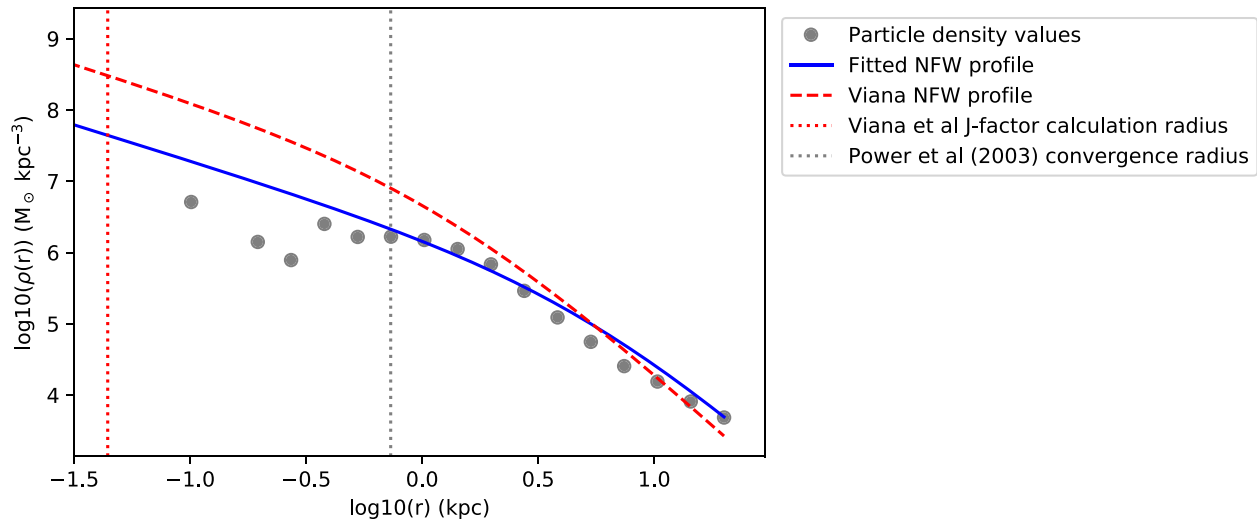
Figure 11. The simulated particle density profile as a function of the radius *r* from the centre of the simulated Sgr DM halo, with the fitted NFW profile to the simulation particle densities (in blue) and the NFW profile fitted by Viana et al. (2012) to stellar velocity dispersion data (in red). The Power et al. (2003) convergence radius $r_c = 0.73$ kpc of the simulated particle halo is indicated; the radial density profile internal to this radius was not utilized when fitting the NFW profile indicated in blue. Also indicated is the radius $r = 0.044$ kpc, corresponding to a projected circular area of 2×10^{-5} sr, utilized to calculate the J-factor in Viana et al. (2012). Clearly, the fitted NFW profile will provide a significantly lower density estimate at this radius than the NFW profile detailed in Viana et al. (2012), but still overestimates the radial density profile at small radii.

a Gaussian with an additional non-zero constant of the form

$$f(x) = \frac{a}{\sigma\sqrt{2\pi}}\exp\left(\frac{-(x-\mu)^2}{2\sigma^2}\right) + c \qquad (11)$$

The parameters of the distribution functions fitted to these scaled 1D projected ρ_s and ρ_{DM}^2 profiles are detailed in Table 1, along with their FWHM values. Note the considerably larger FWHM values measured for the $\Lambda_\odot$ profiles, with poorer fits, resulting from the extensive tidal disruption of Sgr. The FWHM measurements for the projected 1D ρ_s profiles profiles demonstrate the extended nature of any expected gamma-ray emission from stellar-associated sources in Sgr, with the measured FWHM values for these profiles broadly consistent with the extended emission distribution detected with 8.1σ significance in Crocker et al. (2022). Together, the measured FWHM values for the six profiles listed in Table 1 suggest against assuming a point-source emission profile during the analysis of any gamma-ray emission from Sgr. Extending the ρ_{DM}^2, ρ_s, and J-factor distributions to analyse the Sagittarius Stream will be the subject of Paper II.

4 DISCUSSION: COMPARISON OF J-FACTOR MAGNITUDE WITH PAST STUDIES OF THE SAGITTARIUS DWARF

Only a few studies have estimated the J-factor value of the Sgr dark matter component; these estimates are consistently larger than the J-factor value $J_{Sgr} = 1.48 \times 10^{10}$ M$_\odot^2$ kpc^{-5} calculated in this work. We will explore several of these works and compare them to our own calculations in turn.

First, Abramowski et al. (2014) calculate a J-factor value of $J_{Sgr,Abramowski} \simeq 2.9 \times 10^{12}$ M$_\odot^2$ kpc^{-5}, estimating the dark matter density profile utilizing an NFW profile fit to stellar velocity measurements. They then utilize a maximum-likelihood process to determine the most probable contribution of this dark matter distribution toward gamma-ray counts observed with the H.E.S.S.

telescope. Abramowski et al. (2014) marginally detect Sgr with a 2.05σ significance, however conclude that gamma-ray counts due to the dark matter population of Sgr (as opposed to astrophysical sources) are likely negligible.

Secondly, Viana et al. (2012) fit an NFW profile to Sloan Digital Sky Survey stellar velocity dispersion data. This profile is integrated within an integration area of $\Delta\Omega = 2 \times 10^{-5}$ sr $= 0.07$ deg^2 to derive a J-factor value of $J_{Sgr,Viana} = 2.0 \times 10^{16}$ M$_\odot^2$ kpc^{-5}, with uncertainties of a factor of 2.

Given the lack of detection of higher predicted dark matter J-factor fluxes in Viana et al. (2012) and Abramowski et al. (2014), and significantly stronger observed gamma-ray emission from MSP candidates in Sgr (Crocker et al. 2022), the derived J-factor value for Sgr in this study is unlikely to improve current constraints on gamma-ray emission from the Sgr dark matter distribution.

To investigate the discrepancy between this study and the larger J-factor value for Sgr reported in Viana et al. (2012) we fitted an NFW profile of the form (Navarro, Frenk & White 1997)

$$\rho(r) = \frac{\delta_c}{(r/r_s)(1 + r/r_s)^2} \qquad (12)$$

to the simulated radial DM mass density profile (calculated as the mass density of concentric shells), where $\rho(r)$ M$_\odot$ kpc^{-3} is the density at a radial distance of *r* kpc, δ_c is the characteristic density of the halo, and r_s is the scale radius of the halo. As a precaution, only particles at a radius of greater than the Power et al. (2003) convergence radius $r_c = 0.73$ kpc from the centre of Sgr were utilized in the fitting procedure to avoid potentially unrealistic density profiles due to simulation artefacts. The fitted NFW density profile and simulated particle density profile are detailed in Fig. 11 as a function of the radius *r* from the centre of the simulated DM halo. The radial density profile at smaller radii is significantly overestimated by the fitted NFW profile. Thus, relaxing this fitting constraint and fitting the radial density profile at smaller radii would result in shallower inner NFW profile slope and inner profile density values, with

Table 2. The parameters of the NFW profiles either utilized in Viana et al. (2012) or fitted to the simulated particle density profile in this study, with the J-factor values calculated from these profiles utilizing the analytic J-factor definition detailed in equation (13) (see Section 4). The projected area of integration was $\Delta \Omega = 2 \times 10^{-5}$ sr in both cases. The errors quoted are one standard deviation on the fitted parameters.

Parameters	r_s (kpc)	δ_c ($M_\odot$ kpc^{-3})	J-factor value ($M_\odot^2$ kpc^{-5})
Viana et al. (2012)	1.3	1.1×10^7	1.1×10^{16}
Fitted	6 ± 2	$(3 \pm 2) \times 10^4$	2.5×10^{14}
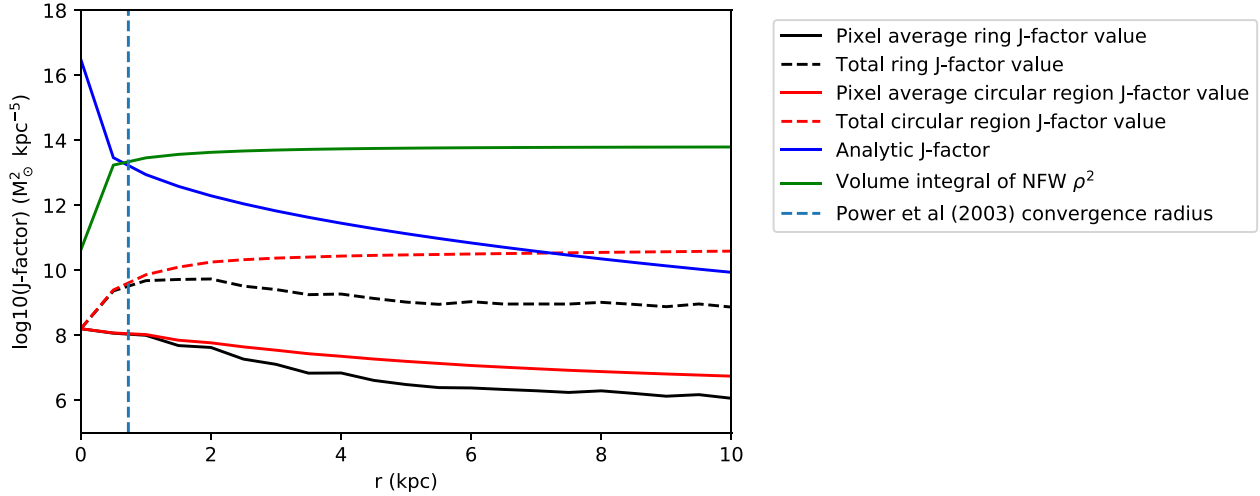
Figure 12. J-factor values for Sgr, as a function of radius r from the centre of the simulated DM halo, computed utilizing various definitions. 'Ring' J-factor values are computed utilizing equation (6), summing particles along the line of sight in a thin ring of radius r kpc centred on Sgr. 'Circular region' J-factor values are also computed utilizing equation (6), summing over all particles along the line of sight within a circular region of radius r kpc centred on Sgr. The analytic J-factor value is computed utilizing equation (13) from the fitted NFW profile depicted in Fig. 12. Also shown in green is the volume integral of the fitted NFW ρ_{DM}^2 profile within a spherical volume of radius r kpc centred on Sgr, computed utilizing equation (14).

corresponding downward revision of any J-factor value estimated from the fitted NFW profile. The fitted NFW profile parameters and the equivalent NFW profile parameters utilized in Viana et al. (2012) are detailed in Table 2.

A J-factor value was calculated from the fitted NFW profile utilizing the equation

$$J(R) = 2 \int_R^{\sqrt{r_d^2 + R^2}} \frac{r \rho^2(r)}{\sqrt{r^2 - R^2}} \, dr \tag{13}$$

where $\rho(r)$ was the NFW density profile given by equation (12) with 'Fitted' parameters detailed in Table 2. r_d is a dark matter density profile truncation radius; we adopt the radius of $r_d = 4$ kpc assumed by Viana et al. (2012) for the purposes of comparison, though variation of this value causes negligible change in our results. Following Viana et al. (2012), a radius of $R = 0.044$ kpc was utilized, equivalent to a projected circular area of $\Delta \Omega = 2 \times 10^{-5}$ sr at the distance of Sgr. This corresponds to a projected angular radius of $0.1°$. The resulting J-factor value calculated with equation (13) was $J_{\mathrm{Sgr,NFW}} = 2.5 \times 10^{14}$ $M_\odot^2$ kpc^{-5}. It is important to note that this J-factor value is independent of the assumed particle-based J-factor definition.

Repeating the calculation detailed in Section 3.1, the lower limit on the WIMP particle annihilation cross-section required to explain the gamma-ray photon flux attributed to Sgr in Crocker et al. (2022), assuming this NFW J-factor value, is also inconsistent with current

constraints (Abazajian et al. 2020; Evans et al. 2023) for WIMP masses $\gtrsim 10$ GeV.

Calculating a J-factor value using equation (13) and an identical radius from the NFW profile $\rho(r)$ defined by the parameters of Viana et al. (2012) yielded a J-factor value of 1.1×10^{16} $M_\odot^2$ kpc^{-5}. This is consistent within errors of the value $J_{\mathrm{Sgr,Viana}} = 2 \times 10^{16}$ $M_\odot^2$ kpc^{-5} reported in Viana et al. (2012), though our calculation uses a different J-factor definition. This in turn implies that the difference between the total J-factor value calculated from the fitted NFW profile $J_{\mathrm{Sgr,NFW}} = 2.5 \times 10^{14}$ $M_\odot^2$ kpc^{-5} and the result of Viana et al. (2012) can be partially explained by the relatively lower density of our fitted NFW density profile at small radii, as evident in Fig. 11 (noting that the J-factor scales as density squared).

To further explore the effect of differing J-factor definitions on the calculated J-factor value for Sgr, the value of the J-factor as a function of radius r from the centre of the simulated DM halo was calculated utilizing both the analytic definition detailed in equation (13) and the J-factor calculated from the pixel summation process detailed in equation (6). The analytic J-factor values were calculated from a radius of $r \geq 0.001$ kpc, comparable to the physical pixel width at the distance of Sgr, namely 0.0035 kpc. These are detailed in Fig. 12. The 'circular region' J-factor values (indicated in solid red) are calculated utilizing equation (6), summing pixel contributions within a circular-based conical area of radius r at the distance of Sgr. The 'ring' J-factor values (indicated in solid black) are again calculated utilizing equation (6) but summing pixels along the circumference of a thin ring of radius r. As would be expected, this approaches

the circular region J-factor value for small radii. The average J-factor value per pixel for both the circular summation regions (in red dashes) and the ring summation regions (in black dashes) are also displayed. In blue on Fig. 12 is the J-factor value calculated with equation (13) from the NFW density profile $\rho(r)$ fitted to the simulated dark matter particle density profile (Fig. 11), implemented utilizing a modified variant of the _SURFACEDENSITY method from the COLOSSUS package (Diemer 2018). Lastly, in green the volume integral of density squared

$$\int \rho^2 \, \mathrm{d}V = 4\pi \int_0^r \rho^2(r)r^2 \, \mathrm{d}r \tag{14}$$

is displayed, again calculated utilizing the NFW density profile $\rho(r)$ fitted to the dark matter particle density profile. Note that, in contrast to this study, the volume integral of density squared is also defined as the J-factor value in Stoehr et al. (2003).

As previously detailed, the 'total circular region J-factor value' detailed in Fig. 12, as calculated with equation (6), was selected to calculate the Sgr J-factor value in this study. The following considerations motivated this selection over other definitions. First, utilizing a simulation-based particle summation J-factor definition likely more accurately accounts for the extended, irregular shape of the Sgr dark matter halo due to tidal disruption (Łokas et al. 2010). Calculating the J-factor value directly from the simulated particle distribution rather than fitting stellar tracers or a profile also avoids assumptions of dynamical equilibrium or spherical symmetry, which are clearly invalid in the case of Sgr. Given the extrapolated NFW profile clearly overestimates the particle density profile in the inner region of the simulated Sgr halo, the particle-based J-factor value is again a conservative lower limit accounting for potential overestimation due to an overestimated fitted NFW profile density. However, some of the density discrepancy between the fitted NFW and particle-based density profiles at small radii *may* result from *potentially* insufficient simulation resolution at small radii. In contrast, the J-factor value calculated from the fitted NFW profile likely exceeds the true J-factor value for Sgr, given the overestimate of the fitted NFW profile to the simulated particle density profile at small radii, in addition the divergent behaviour of the NFW density profile and analytic J-factor definition at small radii.

Secondly, in accordance with equation (6) it is clear that the J-factor definition should exhibit a similar behaviour as a function of radius as the volume integral of density squared, particularly for small radii, as all particles are at a similar heliocentric distance. The pixel averaged ring and pixel averaged circular definitions do not follow this behaviour, nor does the analytic definition detailed in equation (13) which shows a non-physical divergence at small radii. Lastly, the ring J-factor value does not serve to calculate the total integrated J-factor value within an extended structure, as required by this study.

Consideration of these different J-factor definitions also provides additional insight into potential causes for the discrepancy between the Sagittarius Dwarf J-factor value calculated in this study and prior results, such as that reported in Viana et al. (2012). The analytic J-factor definition detailed in equation (13), which reproduces the result of Viana et al. (2012) (within the margin of error) at a radius of $r = 0.044$ kpc from the centre of the simulated DM halo, is clearly divergent at such small radii when calculated utilizing a fitted NFW profile. This is a source of discrepancy between the J-factor value calculated from simulated particle data using equation (6) and the J-factor value for Sgr calculated in Viana et al. (2012) (and other prior works) in addition to the aforementioned discrepancy resulting from the differing density profiles.

Similarly to Viana et al. (2012), an estimate of the dark matter density derived through Jeans analysis is utilized by Evans et al. (2023) to compute a J-factor value of $J_{\mathrm{Sgr,Evans}} = 9.13 \times 10^{12}$ $M_\odot^2$ kpc^{-5} ($10^{19.6}$ GeV cm^{-5}). The analysis of Evans et al. (2023) does not explore the possibility of extended emission beyond a radius of $2°$ from the centre of the Sgr and assumes an NFW profile of small-scale radius ($r_\mathrm{s} = 1$ kpc). We have shown that the DM density distribution of Sgr is significantly extended and find the NFW profile fitted to the Sgr DM density profile has a significantly larger scale radius than assumed in Evans et al. (2023) and Viana et al. (2012). The simulated DM radial density profile (displayed in Fig. 11) indicates a significantly lower core DM density than utilized in Evans et al. (2023) and Viana et al. (2012) is appropriate for Sgr. This, in addition to the significant tidal disruption of the simulated Sgr halo over a large radial range, reinforces the conclusion of Evans et al. (2023) that their DM density profile derived using Jeans analysis likely significantly overestimates the J-factor value of Sgr.

Computing the J-factor value of Sgr utilizing the simulated particle density profile, as detailed in this study, results in a significantly lower J-factor value for Sgr than found in Evans et al. (2023) and implies a DM cross-section incompatible with the DM mass/annihilation cross-section constraints illustrated in Evans et al. (2023, fig. 7), further demonstrating that the Sgr halo should not be utilized for indirect DM detection searches.

5 SUMMARY AND CONCLUSIONS

An N-body/hydrodynamic simulation of the infall and tidal disruption of the Sagittarius Dwarf Galaxy around the Milky Way was utilized to investigate the expected integrated J-factor value of Sgr and explore the morphological characteristics of the projected J-factor distribution. The simulation of Tepper-García & Bland-Hawthorn (2018) was utilized to produce J-factor distributions for the dark matter population of Sgr through a summation of particle density, distance and mass values in line-of-sight pixels. Utilizing this methodology provides a more accurate model of the Sgr DM halo than derivations utilizing stellar tracers through more accurately accounting for the strong tidal disruption of the Sgr DM halo. The markedly extended nature of the J-factor distributions imply the extended nature of any gamma-ray source associated with the Sgr DM halo.

The J-factor value for Sgr, $J_{\mathrm{Sgr}} = 1.48 \times 10^{10}$ $M_\odot^2$ kpc^{-5} (6.46×10^{16} GeV cm^{-5}), was calculated by summing the pixel J-factor values within the core radius of Sgr reported in Majewski et al. (2003). To explain the recently observed gamma-ray emission from Sgr documented in Crocker et al. (2022) with the derived J-factor value for Sgr would require a DM annihilation cross-section incompatible with existing constraints. In conjunction with the recently observed gamma-ray signal from MSP sources in Crocker et al. (2022), this J-factor value militates against the use of Sgr for indirect DM detection experiments.

J-factor distributions were derived to provide insight into the morphology of potential dark matter annihilation signatures as a potential discriminant to astrophysical sources. The relative magnitude of the J-factor distributions at the centre of the Sgr halo and at the core radius of Majewski et al. (2003) indicate that the DM J-factor distribution is insufficiently peaked to explain the morphology of the gamma-ray emission from Sgr observed in Crocker et al. (2022), further indicating that DM annihilation is unable to explain the gamma-ray emission observed in Crocker et al. (2022). Comparison of these distributions with fitted functions indicate low contamination from

potentially spurious small-scale variation in the simulated J-factor distributions.

This calculated J-factor value for Sgr is lower than the J-factor values reported in prior studies (e.g Viana et al. 2012; Abramowski et al. 2014). To provide an indicative comparison between different J-factor definitions, analytic and various particle-based definitions were computed based on the simulated DM radial density profile. We show that the low J-factor value is due to differing density profiles for Sgr and a different J-factor definition, motivated by more accurate modelling of the tidally disrupted Sgr DM density profile.

Whilst the computed J-factor distribution militates against the use of Sgr in indirect DM detection searches, in future work we plan to determine the overall magnitude of the Sagittarius Stream J-factor and investigate its morphological characteristics with a view to probing Fermi-LAT data for potential gamma-ray products of DM annihilation in the Sagittarius Stream.

ACKNOWLEDGEMENTS

DATA AVAILABILITY

No new data were generated or analysed in support of this research.

REFERENCES

Abazajian K. N., Horiuchi S., Kaplinghat M., Keeley R. E., Macias O., 2020, Phys. Rev. D, 102, 043012

Abramowski A. et al., 2014, Phys. Rev. D, 90, 112012
Aharonian F. et al., 2008, Astropart. Phys., 29, 55
Albert A. et al., 2017, ApJ, 834, 110
Astropy Collaboration 2013, A&A, 558, A33
Astropy Collaboration 2018, AJ, 156, 123
Astropy Collaboration 2022, ApJ, 935, 167
Atwood W. B. et al., 2009, ApJ, 697, 1071
Belokurov V. et al., 2013, MNRAS, 437, 116
Bertone G., Hooper D., Silk J., 2005, Phys. Rep., 405, 279
Bringmann T., Weniger C., 2012, Phys. Dark Universe, 1, 194
Calore F., Cholis I., McCabe C., Weniger C., 2015, Phys. Rev. D, 91, 063003
Charbonnier A. et al., 2011, MNRAS, 418, 1526
Crocker R. M. et al., 2022, Nature Astronomy, 6, 1317
Diemer B., 2018, ApJS, 239, 35
Dierickx M. I. P., Loeb A., 2017, ApJ, 836, 92
Evans A. J., Strigari L. E., Svenborn O., Albert A., Harding J. P., Hooper D., Linden T., Pace A. B., 2023, MNRAS, 524, 4574
Garrett K., Dūda G., 2011, Adv. Astron., 2011, 968283
Geringer-Sameth A., Koushiappas S. M., Walker M. G., 2015, Phys. Rev. D, 91, 083535
Goodenough L., Hooper D., 2009, preprint (arXiv:0910.2998)
Gordon C., Macías O., 2013, Phys. Rev. D, 88, 083521
Górski K. M., Hivon E., Banday A. J., Wandelt B. D., Hansen F. K., Reinecke M., Bartelmann M., 2005, ApJ, 622, 759
Hernquist L., 1990, ApJ, 356, 359
Ibata R. A., Wyse R. F. G., Gilmore G., Irwin M. J., Suntzeff N. B., 1997, AJ, 113, 634
Jiang I.-G., Binney J., 2000, MNRAS, 314, 468
Jungman G., Kamionkowski M., Griest K., 1996, Phys. Rep., 267, 195
Kazantzidis S., Łokas E. L., Callegari S., Mayer L., Moustakas L. A., 2011, ApJ, 726, 98
Kuhlen M. , 2010, Advances in Astronomy, 2010
Law D. R., Johnston K. V., Majewski S. R., 2005, ApJ, 619, 807
Law D. R., Majewski S. R., 2010, ApJ, 714, 229
Law D. R., Majewski S. R., Skrutskie M. F., Johnston K. V., 2004, in Prada F., Martinez Delgado D., Mahoney T. J., eds, ASP Conf. Ser. Vol. 327, Satellites and Tidal Streams. Astron. Soc. Pac., San Francisco, p. 239,
Levenberg K., 1944, Quart. Appl. Math., 2, 164
Łokas E. L., Kazantzidis S., Majewski S. R., Law D. R., Mayer L., Frinchaboy P. M., 2010, ApJ, 725, 1516
Macias O., Gordon C., Crocker R. M., Coleman B., Paterson D., Horiuchi S., Pohl M., 2018, Nat. Astron., 2, 387
Macias O., Horiuchi S., Kaplinghat M., Gordon C., Crocker R. M., Nataf D. M., 2019, J. Cosmol. Astropart. Phys., 2019, 042
Majewski S. R., Skrutskie M. F., Weinberg M. D., Ostheimer J. C., 2003, ApJ, 599, 1082
Marquardt D. W., 1963, J. Soc. Ind. Appl. Math., 11, 431
Mazziotta M. N., Loparco F., de Palma F., Giglietto N., 2012, Astropart. Phys., 37, 26
Navarro J. F., Frenk C. S., White S. D. M., 1997, ApJ, 490, 493
Newberg H. J., Carlin J. L. eds, 2016, Astrophysics Space Science Library, Vol. 420, Tidal Streams in the Local Group and Beyond. Springer International Publishing, Switzerland
Pohl M., Macias O., Coleman P., Gordon C., 2022, ApJ, 929, 136
Power C., Navarro J. F., Jenkins A., Frenk C. S., White S. D. M., Springel V., Stadel J., Quinn T., 2003, MNRAS, 338, 14
Rico J., 2020, Galaxies, 8 25
Stoehr F., White S. D. M., Springel V., Tormen G., Yoshida N., 2003, MNRAS, 345, 1313
Tepper-García T., Bland-Hawthorn J., 2018, MNRAS, 478, 5263
Teyssier R., 2002, A&A, 385, 337
Viana A. et al., 2012, ApJ, 746, 77
Virtanen P. et al., 2020, Nat. Methods, 17, 261

APPENDIX A: EQUIVALENCE OF THE J-FACTOR DEFINITION

In Section 2.3, equation (5) defined the J-factor value for a simulated dark matter particle distribution occupying a given volume element. This definition can be shown to be equivalent to the J-factor definition defined in equation (5) of Charbonnier et al. (2011), excepting the factor of $1/4\pi$ introduced in this study to account for the surface area of the flux sphere for each simulation particle involved in the summation detailed in equation (5). Starting with equation (5) of Charbonnier et al. (2011):

$$J = \int_{\Delta\Omega} \int \rho_{\mathrm{DM}}^2(l, \Omega) \mathrm{d}l \, \mathrm{d}\Omega \tag{A1}$$

we first make the change of notation $l = r$ to convert this equation to the notation of this study. It can then be shown that

$$J = \int_{\Delta\Omega} \int \rho_{\mathrm{DM}}^2(r, \Omega) \mathrm{d}r \, \mathrm{d}\Omega = \int \int \rho_{\mathrm{DM}}(r, \Omega)^2 / \left(r^2\right) r^2 \, \mathrm{d}r \, \mathrm{d}\Omega \tag{A2}$$

The right-hand side of equation (A2) is equivalent to an integral over a volume element b of radial length r and angular size $\Delta\Omega$:

$$J_b = \int \int \rho_{\mathrm{DM}}(r, \Omega)^2 / \left(r^2\right) r^2 \, \mathrm{d}r \, \mathrm{d}\Omega = \int_{V_b} \rho_{\mathrm{DM}}^2 / \left(r^2\right) \, \mathrm{d}V \tag{A3}$$

Finally, adding the additional factor of $1/4\pi$ to account for the surface area of the flux sphere for each particle, we reach the J-factor definition defined in the left-hand side of equation (5):

$$J_b = \frac{1}{4\pi} \int_{V_b} \rho_{\mathrm{DM}}^2 / \left(r^2\right) \, \mathrm{d}V = \int_{V_b} \rho_{\mathrm{DM}}^2 / \left(4\pi r^2\right) \, \mathrm{d}V \tag{A4}$$

Accordingly, the J-factor definition defined in equation (5) of Charbonnier et al. (2011) is equivalent to the J-factor definition of equation (5) excepting the differing factor of 4π, when defined for a given volume element b of angular size $\Delta\Omega$ and radial length r.
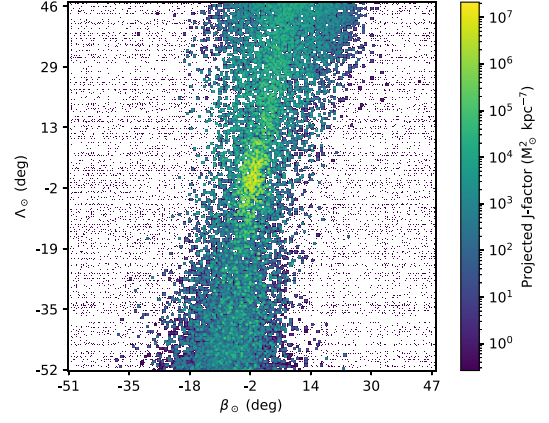
Figure B1. The projected J-factor distribution centred on the location of the simulated Sagittarius Dwarf, again in the coordinate system of Belokurov et al. (2013). This distribution was calculated from the DM J-factor distribution depicted in Fig. 4, which had the units of $M_\odot^2 \, \mathrm{kpc}^{-5} \, \mathrm{deg}^{-2}$, by division of each pixel by the factor C_b detailed in equation (7). The adopted pixel size in this figure remains $\alpha^2 = 0.21 \, \mathrm{deg}^2$.
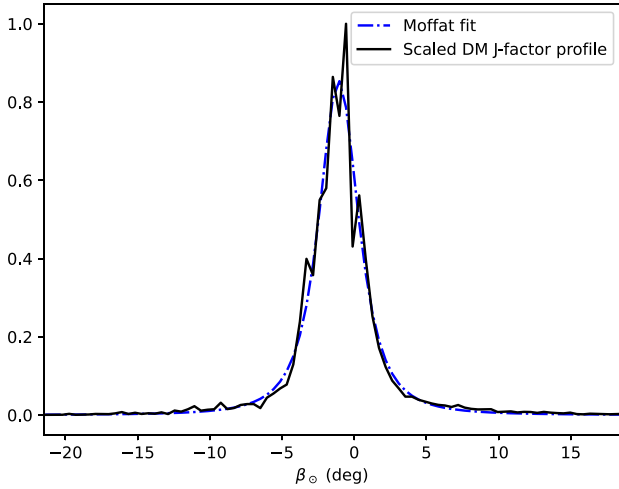
APPENDIX B: THE TWO-DIMENSIONAL J-FACTOR DISTRIBUTION IN PHYSICAL UNITS

Section 2.3 details the production of the projected J-factor distribution of Sgr. As discussed in Section 2.3, the 2D projected J-factor distribution (depicted in Fig. 4) was converted from the angular units of $M_\odot^2 \, \mathrm{kpc}^{-5} \, \mathrm{deg}^{-2}$ to the physical units of $M_\odot^2 \, \mathrm{kpc}^{-7}$ through the division of each pixel b by the factor C_b detailed in equation (7). The resulting projected J-factor distribution is displayed in Fig. B1.
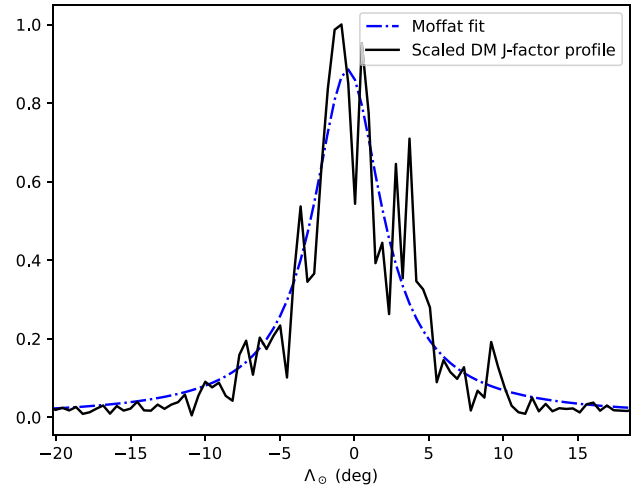
APPENDIX C: SCALED 1D J-FACTOR PROFILES

In Section 3.2, 1D J-factor profiles for Sgr were calculated from the 2D J-factor distribution to illustrate morphological features of the J-factor distribution and inform observational searches. The scaled versions of these profiles were fitted with functions (either a Voigt, Moffat, Gaussian or Gaussian with constant vertical offset) through minimization of the optimization function detailed in equation (9). The parameters of the best-fitting functions are described in Table 1. Only the profiles with angular units (of $M_\odot^2$ kpc^{-5} deg^{-1}) were scaled to avoid any small-scale variation caused by variation in the applied divisor C_b between pixels on profiles with the physical units (namely, $M_\odot^2$ kpc^{-7} deg).

Fig. C1 illustrates the scaled J-factor profile as a function of $\beta_\odot$ whilst Fig. C2 illustrates the scaled J-factor profile as a function of $\Lambda_\odot$. Both of these figures also display the fitted Moffat functions (defined in equation 10).

Figure C2. The dark matter $\Lambda_\odot$ J-factor profile (in the angular units of $M_\odot^2$ kpc^{-5} deg^{-1}), scaled such that the maximum value is equal to 1.0. The adopted $\Lambda_\odot$ bin size remains $0.458°$. The FWHM of the fitted Moffat distribution is $4.9°$.

This paper has been typeset from a TEX/LATEX file prepared by the author.

Figure C1. The dark matter $\beta_\odot$ J-factor profile (in the angular units of $M_\odot^2$ kpc^{-5} deg^{-1}), scaled such that the maximum value is equal to 1.0. Also shown is the fitted Moffat distribution. The FWHM of this fitted distribution is $3.7°$. The adopted $\beta_\odot$ bin size remains $0.458°$.